

# Understanding Intracellular Transport Processes Pertinent to Synthetic Gene Delivery via Stochastic Simulations and Sensitivity Analyses

Anh-Tuan Dinh, Chinmay Pangarkar, Theo Theofanous, and Samir Mitragotri

Department of Chemical Engineering, University of California, Santa Barbara, California

**ABSTRACT** A major challenge in synthetic gene delivery is to quantitatively predict the optimal design of polymer-based gene carriers (polyplexes). Here, we report a consistent, integrated, and fundamentally grounded computational methodology to address this challenge. This is achieved by accurately representing the spatio-temporal dynamics of intracellular structures and by describing the interactions between gene carriers and cellular components at a discrete, nanoscale level. This enables the applications of systems tools such as optimization and sensitivity analysis to search for the best combination of systems parameters. We validate the approach using DNA delivery by polyethylenimine as an example. We show that the cell topology (e.g., size, circularity, and dimensionality) strongly influences the spatiotemporal distribution of gene carriers, and consequently, their optimal intracellular pathways. The model shows that there exists an upper limit on polyplexes' intracellular delivery efficiency due to their inability to protect DNA until nuclear entry. The model predicts that even for optimally designed polyethylenimine vectors, only ~1% of total DNA is delivered to the nucleus. Based on comparison with gene delivery by viruses, the model suggests possible strategies to significantly improve transfection efficiencies of synthetic gene vectors.

## INTRODUCTION

Polymer-based systems are being extensively studied as carriers for gene therapy (1), and have also been used in clinical trials (2). Despite the obvious advantages of safety and malleability over viral vectors, polymer-based vectors (polyplexes) have not been very successful at the clinical level owing to their poor delivery efficiency. Even the best polyplexes are 1000-fold less effective than typical viral vectors such as adenoviruses. This poor efficiency stems from the numerous intracellular barriers that retain or destroy a majority of the gene dose before it can reach the host nucleus (3). A central challenge in the field is identification and synthesis of a polymer that can enhance translocation of the polyplex across these barriers. To this end, a large number (literally thousands) of polymers have been evaluated—poly-imines (4), dendrimers (4), polyamino esters (5), chitosans (6), and cyclodextrins (7), to name a few. However, only a few of these have been found to be significantly better than polyethylenimine (PEI<sup>25kDa</sup>), the accepted standard in polymer-based gene delivery. Further, it is not clear whether these polymers, many of which have been developed and optimized for use with cultured cells, will be effective in clinical applications.

The low transfection efficiency of synthetic vectors leads to a key question: Is there an inherent limitation to polyplexes? Or have we not found the magic polymer yet? Two challenges need to be addressed before this question can be answered. The first challenge, biological in nature, involves

developing the design criteria of polyplexes that will lead to maximum efficiency. The second challenge, chemical in nature, involves design and synthesis of polymers that will form such polyplexes.

In this article, we exclusively address the first challenge. There are two major issues that make this task difficult. The first issue stems from fragmented understanding of intracellular trafficking of polyplexes, mainly due to the strong dichotomy in the experimental approaches used. One approach is based on macroscopic measurements of the delivery efficiency using *in vitro* transfection assays. The other approach is based on measurements at the single-cell single-particle level. Macroscopic experiments do not provide in-depth mechanistic understanding of the events leading to the final effect. Single particle data, on the other hand, aim to quantify individual transport steps (8,9), many of which, such as escape from endosomes, remain tremendously difficult to visualize due to the rare and random nature of these events (8). The link between these two distinct scales (i.e., macroscopic and microscopic) is still missing. The second outstanding issue is the limited knowledge of the structure-activity relationships that link vector's physico-chemistry to the efficiency of individual trafficking steps. This limitation confounds systematic experimental optimization of vector properties.

We address the problem of understanding and optimizing intracellular transport by developing a detailed mathematical model of the gene delivery pathway. Previous models of gene delivery have essentially followed a pharmacokinetic approach (10–13), which treats the cell as a well-mixed compartment. The major shortcoming of kinetic models is that they approximate all spatial and transport processes by kinetic equations. The kinetic rate constants have to be

---

*Submitted August 21, 2006, and accepted for publication October 17, 2006.*

Anh-Tuan Dinh and Chinmay Pangarkar contributed equally to this work. Address reprint requests to Prof. Samir Mitragotri, Dept. of Chemical Engineering, University of California, Santa Barbara, CA 93106. Tel.: 805-893-7532; E-mail: samir@engineering.ucsb.edu.

© 2007 by the Biophysical Society

0006-3495/07/02/831/16 \$2.00

---

doi: 10.1529/biophysj.106.095521

obtained by fitting the model to experimental data. This makes it difficult to extrapolate the results of the model predictions. Most importantly, kinetic models, due to their simple approximations of intracellular transport, fail to take advantage of the wealth of data made available by single-particle tracking experiments.

We realize that much of the complexity of the vector-cell system arises from the spatio-temporal variation in the rates of various intracellular processes and can be captured only by considering a spatial view of the cell. To address this challenge, we develop an advanced stochastic simulation framework that effectively describes the dynamic and spatial nature of intracellular trafficking of nanoscale carriers. By providing a realistic representation of topology and dynamic organization of the cell interior, the modeling framework serves as a three-dimensional, “live,” computer-constructed cellular map for navigation of nanoscale carriers. The model contains information from the shortest to the longest relevant length and timescales, and wherever possible, is rigorously validated against experimental data. Wherever mechanistic or quantitative information in the literature is incomplete, we perform systematic experiments to measure the required processes. We use the model to calculate the delivery efficiency—the probability that a polyplex, upon internalization, successfully delivers DNA to the host nucleus, and to predict the optimal intracellular itinerary. We show that the optimal pathway is controlled by several cell-specific properties such as cell morphology, endocytic trafficking, and microtubule-dependent transport.

## EXPERIMENTAL METHODS

### Polyplexes

Polyethylenimine (25 kDa) was obtained from Sigma (St. Louis, MI). All fluorescent dyes (Oregon green, TMR-Dextran, 70 kDa) were obtained from Molecular Probes (Eugene, OR). Amine groups on polyethylenimine (25 kDa) were labeled using the succinimidyl ester of Oregon green as per the manufacturer's protocol. The complexes were always prepared at a Nitrogen/Phosphorus ratio of 9, in 150 mM NaCl solution. Complexes were used between 30 and 45 min post-synthesis. They were verified to transfect skin fibroblasts.

### Cell culture and transfection

Human Skin Normal fibroblasts (ATCC, TE.353.Sk, Manassas, VA) were cultured as per the standard ATCC protocols. Briefly, cells were maintained in Dulbecco's modified eagle's medium (ATCC), which had been supplemented with 4 mM L-glutamine and 1.5 g/L sodium bicarbonate. Cells were grown at 37°C and 5% CO<sub>2</sub>; and maintained in the log phase by consistent subculture. On the day before the experiment, cells were seeded onto a glass bottom petri dish at a density of ~7000–10,000 cells/cm<sup>2</sup>. The next day, complexes were added to serum-free medium at a concentration of 2 µg DNA/ml. The cells were incubated with this medium for 15–30 min at 37°C. Post-incubation, the unbound particles were washed away 5× by phosphate-buffered saline and the cells were replenished with fresh serum containing medium, which was supplemented with 25 mM HEPES to maintain carbonate-bicarbonate balance in the absence of CO<sub>2</sub>.

## Fluorescence microscopy

The cells were placed on the stage of a Zeiss (Thornwood, NY) Axiovert-25 inverted microscope, which was fitted with a Biopetechs Delta T temperature controller (Biopetechs, Butler, PA). The cells were observed using an oil immersion 100× objective. Oregon green was excited and observed using HQ480/40× and HQ 555/40M FITC compatible filters from Chroma (Rockingham, VT). For every cell, bright-field and fluorescence images were acquired using a cooled CCD-camera (CoolSNAP<sub>HQ</sub>, Roper Scientific, Duluth, GA) which was controlled by Metamorph imaging software (Universal Imaging, Downingtown, PA). The images were acquired for 1–2 min at 1 frame per second.

## Immunofluorescence

Lysosomes in the cells were immunolabeled using standard techniques. Briefly, the cells were fixed for 30 min using freshly prepared 2% paraformaldehyde. This was followed by permeabilization with 0.01% Tween-20 in phosphate-buffered saline and blocking with 2% BSA for 2 h. The cells were then labeled with mouse monoclonal anti-Lamp1 (primary antibody, BD Biosciences) and subsequently with Rhodamine red-X-Goat anti-mouse IgG (secondary antibody, R6393, Molecular Probes). The cells were then mounted using VectaShield (Vector Labs, Burlingame, CA). Rhodamine-X labeled antibodies were observed using HQ 545/30X and HQ 640/50M filters from Chroma.

## Image processing and analysis

All image acquisition and processing steps were performed within the Metamorph software. Phase contrast images of cells were used to extract coordinates of the cell membrane and nuclear membrane. The raw fluorescence images show bright punctuate structures corresponding to diffraction-limited images of fluorescent vectors. Images were processed with a custom FFT-based protocol to filter out very long-range and very short-range correlations. This was followed by a series of Gaussian blurring, convolution, and unsharp masking steps until the resultant image could be thresholded such that most of the bright structures could be individually measured. All particle coordinates were exported to MS Excel (Microsoft, Redmond, WA). All further calculations involving cell shape, vector distribution, etc., were performed in MatLab (The MathWorks, Natick, MA). For single particle tracking, stacks of fluorescent images of cells were filtered to remove high frequency noise. Other filtering steps were avoided to preserve the intensity structure of the raw image. Trajectories of all the particles were individually verified by replaying the video with the trajectory superimposed on the image. The coordinates of a vector in all the frames were exported to MS Excel, and were used for all further calculations. Colocalization of Oregon green labeled PEI25-DNA vectors and anti-Lamp-1 labeled lysosomes was measured by overlaying the Red and Green channel images. The images were self-normalized using standard histogram-stretching methods. Colocalization was considered significant if the Red and Green structures had >85% of their combined pixels in common.

## STOCHASTIC SIMULATIONS

The objective of stochastic simulations is to bring-out the spatial and physical aspects of intracellular trafficking of polyplexes by providing a realistic representation of cell geometry and intracellular organization and a discrete and mechanistic description of transport processes. As in single-particle tracking experiments, the proposed model follows the trajectories of polyplexes inside cells. The computational domain is defined by the cell geometry, which is reconstructed from experimental visualization of cells (see below).

We distinguish between *in vitro* and *in vivo* experiments. Many cells, especially those considered in this analysis (human skin fibroblasts) spread on the substrate under *in vitro* conditions, and the cell thickness is often much smaller than other dimensions due to adhesion to the surface. Therefore, it is sufficient to formulate the simulations in two dimensions for *in vitro* applications (Fig. 1 *a*). *In vivo* applications, however, require considerations of three-dimensional geometry (Fig. 1, *b–d*).

The positions and the biophysical states of polyplexes are updated using a stochastic algorithm. Fundamentally, all stochastic events simulated here can be classified into two categories: 1), transport events; and 2), reaction events. Transport events (diffusion or motor-driven movements) are captured by equations of motion. Reaction events, involving association, dissociation or rupturing of entities, are approximated as first-order Markov processes. Definitions of variables and symbols are summarized in Table 1.

## Mathematical description of cellular environments

### Cell geometry

For *in vitro* applications, we reconstruct cell geometries from phase contrast images of cultured human fibroblasts. Viewing from the top, the cell interior is divided into two regions, cytoplasmic and supranuclear, separated by the nuclear

resolution images captured at 100 $\times$  magnification allow for precise determination of the shape of cell and nucleus. For *in vivo* applications, we reconstruct the cells from histological and electron microscopy images of fibroblasts embedded in tissues. The procedure for *in vivo* cells is more complicated and described in detail in the Supplementary Material. The cell geometry is represented by two surfaces describing the cell membrane and the nuclear envelope (see Fig. 1 *b*). Our reconstructed three-dimensional cells are in good agreement with past descriptions of fibroblasts under *in vivo* conditions. All cell geometries remain unchanged during simulations.

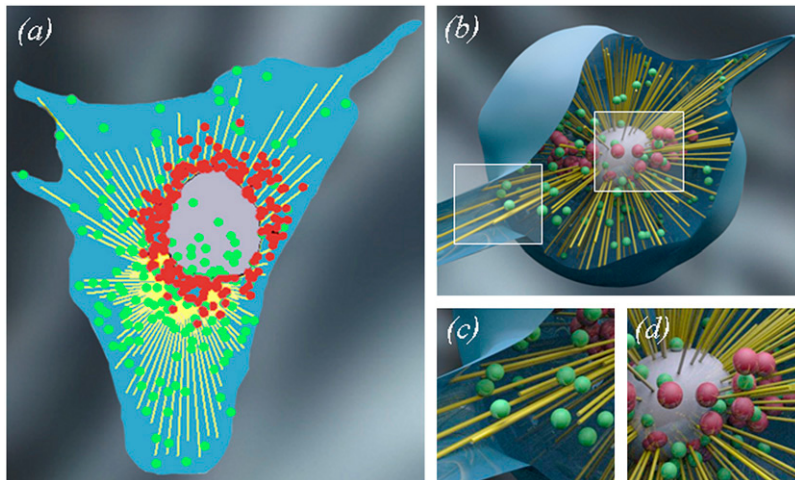
### Microtubules

Microtubules (MTs) exhibit dynamic instability, i.e., stochastic switching between prolonged phases of assembly and rapid phases of disassembly. The frequency of transition from slow assembly to rapid disassembly (referred to as “catastrophe”) determines the stability of the MT population (24). In this model, MTs are modeled as straight lines, which grow radially in random directions from the microtubule-organizing center (MTOC) toward the cell periphery. MTOC is placed randomly in the vicinity of the nucleus. To describe microtubule polymerization dynamics, we use stochastic equations that follow the individual MT length history. A microtubule switches intermittently between three phases (growth, shrinkage, and collapse) as follows (14):

$$l(t + \Delta t) = \begin{cases} l(t) + v_{\text{grow}} \Delta t & \text{for } 0 < q < k_{\text{grow}} \Delta t & \text{(growth)} \\ l(t) - v_{\text{shrink}} \Delta t & \text{for } k_{\text{grow}} \Delta t < q < k_{\text{grow}} \Delta t + k_{\text{shrink}} \Delta t & \text{(shrinkage)} \\ l(t) - ml(t) & \text{for } k_{\text{grow}} \Delta t + k_{\text{shrink}} \Delta t < q < k_{\text{grow}} \Delta t + k_{\text{shrink}} \Delta t + k_{\text{cat}} \Delta t & \text{(catastrophe)} \\ l(t) & \text{for } k_{\text{grow}} \Delta t + k_{\text{shrink}} \Delta t + k_{\text{cat}} \Delta t < q < 1 \end{cases} \quad (1)$$

boundary (see Fig. 1 *a*). We use an image analysis program (Metamorph, Universal Imaging) to extract the coordinates of the nuclear boundary and the cell boundary. The high-

where  $q$  and  $m$  are random numbers between 0 and 1. The values  $k_{\text{grow}}$ ,  $k_{\text{shrink}}$ , and  $k_{\text{cat}}$  are the reaction rate constants for MT growth, shrinkage, and collapse, respectively.



**FIGURE 1** Computer representation of human skin fibroblasts (*a*) *in vitro*, where the cell is represented as a two-dimensional object and (*b*) *in vivo*, where the cell is represented by a three-dimensional structure. Green and red objects represent endosomes and lysosomes respectively. Thin yellow lines represent microtubules (MTs). The microtubule-organizing center (MTOC) is randomly located in the vicinity of the nucleus. For clarity, we use fewer endosomes, lysosomes, and MTs to render the reconstructed cells than in simulations. Two regions of the three-dimensional cell are magnified and shown in panels *c* and *d*.

**TABLE 1** Nomenclature

$A_{\text{cell}}$	Area of a cell.
$c_E, c_L$	Concentration of endosomes and lysosomes (# per unit area).
$c(r, t)$	Normalized local concentration of polyplexes in the cell at distance $r$ from the nuclear boundary at time $t$ post-transfection.
$c_{\text{peri}}$	Normalized local concentration of polyplexes in the perinuclear region, which is defined as a layer of width $2 \mu\text{m}$ around the nucleus.
$c_{\text{supra}}$	Normalized local concentration of polyplexes in the supranuclear region.
$D_{\text{DNA}}$	Diffusivity of DNA in cytoplasm, $\mu\text{m}^2/\text{s}$ .
$D_E$	Diffusivity of endosomes, $\mu\text{m}^2/\text{s}$ .
$D_{L,f}, D_{L,c}$	Diffusivities of free and clustered lysosomes, $\mu\text{m}^2/\text{s}$ .
$\Phi(t)$	Spatially averaged success probability of a vector that escapes at any location in the cytoplasm at time $t$ post-transfection.
$f_{\text{cat}}$	Catastrophe frequency of microtubules, $\text{s}^{-1}$ .
$k_{\pm, S}, k_{\pm, S}^{\perp}$	Rate constant for a particle binding to and detachment from MTs, $\text{s}^{-1}$ .
$k_{\text{cluster}}, k_{\text{de-cluster}}$	Rates of formation and breakup of lysosomal clusters, $\text{s}^{-1}$ .
$k_{\text{escape}}$	Rate constant for escape of vectors from endosomes or lysosomes, $\text{min}^{-1}$ .
$k_{\text{tr}}$	Rate constant for transfer of vectors from endosomes to lysosomes, $\text{min}^{-1}$ .
$k_{\text{unpack}}$	Rate constant for unpacking of vectors in cytoplasm or lysosomes, $\text{min}^{-1}$ .
$k_{\text{int}}$	Rate constant for internalization of vectors via endocytosis, $\text{min}^{-1}$ .
$k_{\text{deg-cyto, DNA}}$	Rate constant for degradation of DNA in the cytoplasm, $\text{min}^{-1}$ .
$k_{\text{nuc}}$	Rate constant for nuclear entry, $\text{min}^{-1}$ .
$k_{\text{degL}}$	Rate constant for degradation of vector in lysosomes, $\text{min}^{-1}$ .
$K_s$	Equilibrium constant for particle binding and unbinding with microtubules ( $s = \pm 1$ )
$\Phi(r)$	Probability that a vector, which escapes from endo/lysosomes at distance $r$ from the nuclear membrane, can successfully deliver DNA into the nucleus.
$\Theta(t)$	Probability that a vector, which escapes from endo/lysosomes at time $t$ post-transfection, can successfully deliver DNA into the nucleus.
$P_e(t)$	Probability distribution of escape time.
$r$	Distance of a particle from the nuclear boundary, $\mu\text{m}$ .
$\Psi$	Overall delivery efficiency.
$s$	Transport substate (0: diffusion, and $\pm 1$ : toward MT plus and minus ends).
$S_V$	Biophysical state of a vector ( $M$ : cell membrane, $E$ : inside endosomes, $L$ : inside lysosomes, $C$ : inside cytoplasm, and $P$ : unpacked plasmids).
$t$	Time.
$T_f$	Time at which the experiment/simulation is terminated, in hours.
$t_{\text{grow}}, t_{\text{shrink}}$	Mean growth and shrinkage times, s.
$v_{\text{grow}}, v_{\text{shrink}}$	Rates of MT growth and shrinkage, m/s.
$V_{\pm}^S$	MT-dependent velocity of a particle toward plus or minus ends of MTs, $\mu\text{m}/\text{s}$ .

## Mathematical description of intracellular trafficking of polyplexes

We introduce two state variables to characterize intracellular trafficking of polyplexes, namely, biophysical state  $S$ , which indicates the biological compartmentalization and transport state  $s$ , which represents the type of movements of polyplexes.

### Biophysical states

After binding to the cell membrane, the intracellular pathway of a polyplexes can be represented by five distinct biophysical states  $S$ : bound to cell membrane ( $M$ ); inside endosomes ( $E$ ); inside lysosomes ( $L$ ); inside cytoplasm ( $C$ ); and unpacked plasmids ( $P$ ) (Fig. 2). The states correspond to the stages of the gene delivery pathway (see Fig. 2 legend and Supplementary Material, section 1.3).

Transitions from one state to another depend on various biological and physical factors, such as location, interactions with cellular organelles, and physiochemical properties of polyplexes. In the present model, we approximate the transition between two biophysical states of the vectors as a first-order reaction. For instance, we use  $k_{\text{escape}}$  (i.e., the rate of escape from endocytic vesicles) to characterize the transition from  $S = E$  to  $S = C$  (Fig. 2) The probability that

a transition from state  $E$  to state  $C$  occurs in the interval  $[t, t + \Delta t]$  is given by

$$\text{Prob}(S = C, t + \Delta t | S = E, t) = k_{\text{escape}} \Delta t. \quad (2)$$

We then compare a random number uniformly distributed between 0 and 1 to this probability to determine whether or not the event occurs in the time interval  $\Delta t$  (see Supplementary Material, section 1, for more information). Other transitions are predicted in a similar manner.

### Transport states

Each biophysical state has a distinct transport pattern. Membrane-bound and cytoplasmic polyplexes move only via diffusion. On the other hand, polyplexes inside endosomes switch intermittently between diffusion and directional transport. To account for these distinct transport modes, we introduce the concept of transport state  $s$ . Each biophysical state is characterized by a set of transport states and a diagram depicting the transitions between these states. At each point in time, a polyplex occupies one of the movement states. For instance, transport of polyplexes inside endosomes is represented by three transport states,  $s = \pm 1, -1$ , and 0 (+1, plus-end directional transport; -1, minus-end

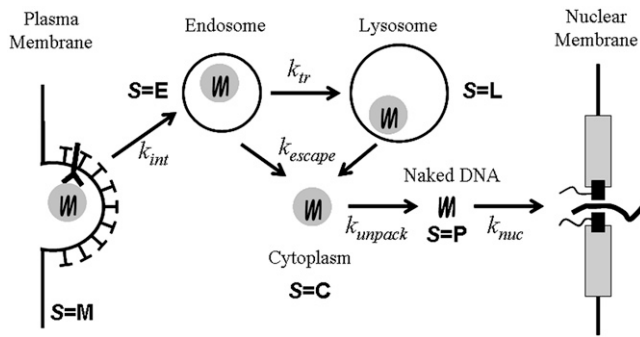


FIGURE 2 Gene delivery pathway of polyplexes. Polyplexes are internalized by endocytosis. They are immediately delivered to endosomes and subsequently to lysosomes. To gain entry to the nucleus, the polyplexes must escape from endosomes or lysosomes. Once inside the cytoplasm, the polyplexes unpack to release the DNA for successful nuclear entry. Ultimately, the exogenous DNA is transcribed, and gene products are synthesized. The biophysical states  $S$  and the rates of transition between them are shown in the figure.

directional transport; and 0, diffusion). We define  $V_{+1}^E$  and  $V_{-1}^E$  as velocities of directional movements toward the plus-end and the minus-end of microtubules. The values  $k_{+1,E}$  and  $k_{-1,E}$  are first-order rate constants characterizing particle's transition from  $s = 0$  to  $s = +1$  and  $s = -1$ , respectively. The values  $k'_{+1,E}$  and  $k'_{-1,E}$  are the rate constants of corresponding reverse processes. Thus, the cytoplasmic transport pattern of endosomes is represented by seven parameters,  $D_0^E$  (free diffusion coefficient),  $V_{+1}^E, V_{-1}^E, k_{+1,E}, k_{-1,E}, k'_{+1,E}$ , and  $k'_{-1,E}$ . These transport coefficients are independent of location inside the cytoplasmic region. Quantitative measurements of movements of PEI-DNA complexes in human fibroblast support this assumption. Table 2 summarizes the transition diagram and the associated transport parameters for all five biophysical states.

The position of a polyplex occupying a diffusive transport state is updated using two- or three-dimensional random walk. For MT-bound entities, the equations of motion are applied,

$$\bar{x}_i = \bar{x}_i + V_{\pm}^i \bar{m}_j \Delta t, \quad (3)$$

where  $\bar{x}_i$  is the position of polyplex  $i$  and  $\bar{m}_j$  characterizes the microtubule  $j$  that the polyplex  $i$  is associated with.

To simulate transitions between biophysical states, we employ the same principle introduced above (see Eq. 2). However, the occurrence of several transition events requires specific physical conditions. For instance, binding of a diffusing endosome to MT only occurs if the endosome is within a radius  $r_c$  from a neighboring MT, and the probability that it will bind to and travel toward the plus- and minus-ends of the MT in an interval  $\Delta t$  are  $k_{+1,E} \Delta t$  and  $k_{-1,E} \Delta t$ , respectively. Similarly, termination of microtubule-dependent runs depend not only on the rates of unbinding,  $k'_{+1,E}$  and  $k'_{-1,E}$ , but also on the physical layout of the microtubule tracks. The endosome will fall off the MT, that is, become diffusive in the next time step, once reaching the ends of the MT or

hitting the nuclear boundary or the cell boundary, which act like solid walls.

The most interesting case is the transition between the clustered state and the free state of polyplexes inside lysosomes. Lysosomes tend to form clusters in the perinuclear region (Fig. 4 *a*, *inset*). When a lysosome-carrying polyplex aggregates with other lysosomes, it exhibits restricted diffusion. When it is free, it can travel bidirectionally along microtubules just like endosomes. The declustering rate,  $k'_{2,L}$ , is presumably space-dependent, while the rate of transition from the free to the clustered state is a function of the normalized clustering rate and the local concentration of lysosomes,  $C_L(r)$ , which is obtained a priori by analysis of lysosome images after immunolabeling.

## Simulation scheme and data analysis

Here, we describe the simulation scheme for in vitro applications. The simulation scheme for in vivo applications is similar. For each simulation, an arbitrary cell configuration is chosen from the library of different cell geometries, which defines the computational domain. During one time-step, the cellular environments and the states/positions of polyplexes are updated according to the following scheme:

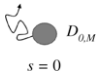
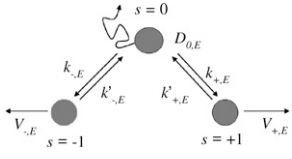
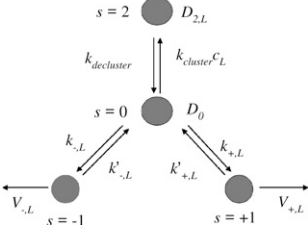

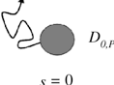
1. Update cellular environments: cell geometry (if desired), and the state (growth, shrinkage, or collapse) and the length of microtubules.
2. Updates of polyplexes: biophysical states, transport states, and polyplexes' locations.

To guarantee accuracy and stability of the numerical scheme, we use a small time step,  $\Delta t = 0.2$  s. The time step is much smaller than the governing timescales of the transport processes. Varying  $\Delta t$  between 0.1 s and 2 s does not significantly influence the model predictions. For each parameter set, we sample 10,000 trajectories from 200 cells. The delivery efficiency is calculated based on the number of DNA molecules that gain entry to the nucleus at a final time  $T_f$ , when we terminate the simulations. The simulation software is available by request.

## PARAMETER ESTIMATION

The model contains a large number of parameters, which describe different aspects of the problem such as cell geometry, microtubules, trafficking of endocytic vesicles, trafficking of vectors in the endocytic pathway, and trafficking of vectors after endosomal/lysosomal escape. We measured parameters describing the trafficking of vectors present within endocytic vesicles using skin-fibroblasts as the model cell-line and PEI<sup>25kDa</sup>-DNA as the vector. However, for the steps after endosomal escape, experimental measurements are not possible at the single particle level. In such cases, data from bulk measurements was used. For example, we adapted the rate of plasmid degradation in the cytoplasm from

**TABLE 2** Transition diagrams and transport parameters for biophysical states

Biophysical state	Transition map	Parameters	Reference
Membrane		$D_{0,M} \sim 0.001 \mu\text{m}^2/\text{s}$	This work.
Endosome		$D_{0,E} \sim 0.0005\text{--}0.001 \mu\text{m}^2/\text{s}$ $V_{+,E} = V_{-,E} = 0.33 \mu\text{m/s}$ $k_{+,E} = k_{-,E} = 0.125 \text{ s}^{-1}$ $k_{+,E}' = k_{-,E}' = 0.3 \text{ s}^{-1}$	This work.
Lysosome		$D_{0,L} = 0.0001 \mu\text{m}^2/\text{s}$ $V_{+,L} = V_{-,L} = 0.56 \mu\text{m/s}$ $k_{+,L} = k_{-,L} = 0.05 \text{ s}^{-1}$ $k_{+,L}' = k_{-,L}' = 0.33 \text{ s}^{-1}$ $k_{\text{de-cluster}} = 0.125 \text{ s}^{-1}$ $k_{\text{cluster}} = 0.5 \text{ s}^{-1}$	This work.
Cytoplasmic		$D_{0,C} \sim 0.001 \mu\text{m}^2/\text{s}$	Estimated based on Stokes-Einstein relationship.
Plasmid		$D_{0,P} \sim 0.001 \mu\text{m}^2/\text{s}$	(17)

Lechardeur et al. (15), who measured degradation of injected plasmids using fluorescence in situ hybridization.

### Microtubule organization and dynamics

Based on immunolabeled images of fibroblasts, we estimate that the number of microtubules in the plane of movements under in vitro conditions to be  $\sim 1000\text{--}1500$ . To our knowledge, microtubule polymerization dynamics in human skin fibroblasts have not been quantified yet. Accordingly, we postulate that the parameters that characterize microtubule dynamic instability in human fibroblasts are similar to those of CHO fibroblasts. Komarova et al. (16) investigated the lifecycle of MTs in CHO cells and reported a growth rate ( $v_{\text{grow}}$ ) of  $0.25\text{--}0.35 \mu\text{m/s}$ , a shortening rate ( $v_{\text{shrink}}$ ) of  $0.3\text{--}0.4 \mu\text{m/s}$ , and a catastrophe frequency ( $f_{\text{cat}}$ ) of  $0.005 \text{ s}^{-1}$ . Also, the mean growth time  $t_{\text{grow}}$  is  $\sim 40\text{--}60 \text{ s}$  and the mean shrinkage time  $t_{\text{shrink}}$  is  $5\text{--}15 \text{ s}$ . Variations of  $v_{\text{grow}}$ ,  $v_{\text{shrink}}$ ,  $t_{\text{grow}}$ , and  $t_{\text{shrink}}$  within the estimated intervals do not significantly affect the predicted particle distributions. The most sensitive parameter is  $f_{\text{cat}}$ , which determines the stability of the microtubule tracks.

### Transport properties of endosomes

The cytoplasmic transport properties of endosomes are represented by seven parameters,  $D_{0,E}$  (free diffusion coefficient),  $V_{+,E}^E$ ,  $V_{-,E}^E$ ,  $k_{+,E}$ ,  $k_{-,E}$ ,  $k'_{+,E}$ , and  $k'_{-,E}$ . These parameters are not available in the literature and are therefore measured from our own experiments (see Supplementary Material, Section 1.2.1).

1. Diffusivity,  $D_{0,E}$ . Trajectories of  $\sim 50$  fluorescently labeled, almost immobile vectors were selected from experimentally measured movements of  $\text{PEI}^{25\text{kDa}}$ -DNA vectors (assuming that vectors are present within endosomes). These trajectories were used to calculate the mean-squared displacement (MSD) as a function of the timescale  $t$ . Based on the MSD, we estimate  $D_{0,E}$  to be  $0.0005\text{--}0.001 \mu\text{m}^2/\text{s}$ . Similar values have been reported previously in the literature. Immunolabeling of endosomes (using anti-rab5, red) showed that all observable green fluorescence of PEI-DNA vectors colocalizes with anti-rab5 at the time of measurements (1 h post-transfection). This confirms that, within experimental errors, the imaged vectors were indeed present within endosomes.

2. Rate of unbinding,  $k'_{\pm,E}$ . The rate of unbinding is the inverse of the mean duration of “spurts” or “runs” in a certain direction. Fig. 3 *a* shows the probability distribution of duration of a run in the plus and minus directions, calculated from  $\sim 250$  active trajectories. The exponential nature of this distribution also supports the assumption of a first-order unbinding process. The run lengths in either direction show identical distributions and thus yield  $k'_{\pm,E} = 0.3 \text{ s}^{-1}$ .
3. Rate of binding,  $k_{\pm,E}$ . At equilibrium, a certain fraction  $f$  of particles must exist in bound states 1 and  $-1$ , and  $f = (k_{+,E}/k'_{+,E} + k_{-,E}/k'_{-,E}) / (k_{+,E}/k'_{+,E} + k_{-,E}/k'_{-,E} + 1)$ . Here  $k_{+,E} = k_{-,E}$  and  $k'_{+,E} = k'_{-,E}$ ; and for  $K = k_{\pm,E}/k'_{\pm,E}$ , we get  $f = 2K/(2K+1)$ . Thus, knowing  $k'_{\pm,E}$ , and measuring  $f$  from time-lapse videos of cells at different times, the rate of binding  $k_{\pm,E}$  can be calculated. For PEI-DNA containing endosomes, the rate of binding calculated from videos over 20–120 min post-transfection is  $\sim 1/8 \text{ s}^{-1}$ .
4. Velocity distribution,  $V_{\pm}^S$ . Endosomes do not exhibit a constant velocity, but a distribution of velocities that ranges from  $<0.05 \mu\text{m/s}$  to  $3 \mu\text{m/s}$ . Fig. 3 *b* shows the distribution of frame-to-frame speeds in both the plus and minus directions. It can be seen that the distributions are identical exponential distributions, with a mean velocity of  $0.33 \mu\text{m/s}$ .

### Transport properties of lysosomes

Lysosomes form clusters and accumulate in the perinuclear region, as illustrated in Fig. 4, *a* and *b*. Lysosomes switch stochastically between free and clustered states, and the properties in each of these states are measured as follows:

1. Transport of free lysosomes. We use the same method as in case of endosomes to obtain  $k'_{\pm,L}$ ,  $k_{\pm,L}$ ,  $v_{\pm,L}$ , and  $D_{f,L}$  for free lysosomes. Lysosomes are labeled by fluorescent dextran (10 kDa), which has been chased into the lysosomes by incubating the cells for 24 h. We confirmed this experimentally by labeling endosomes with lysosome-associated-membrane-protein (lamp)-1. The analysis of the experimental data on lysosome transport yields  $k'_{\pm,L} = 0.33 \text{ s}^{-1}$ ,  $k_{\pm,L} = 1/20 \text{ s}^{-1}$ ,  $v_{\pm,L} = 0.56 \mu\text{m/s}$ , and  $D_{f,L} = 10^{-4} \mu\text{m}^2/\text{s}$ .
2. Transport of clustered lysosomes. Clustered perinuclear lysosomes rarely exhibit directed motion. In the event

that directed motion is seen, it is always followed by dissociation of the lysosomes from the cluster into the free phase. Thus, transport of a lysosome in the clustered phase is described by diffusion ( $D_{c,L} = 10^{-4} \mu\text{m}^2/\text{s}$ ).

3. Transition between free and clustered states. To find the rate at which a free lysosome becomes part of a cluster and vice versa, we examined videos of lysosomal clusters. In every video, a cluster of 4–5 lysosomes was randomly chosen and tracked for a period of 2 min. The cluster is often highly dynamic, with lysosomes constantly leaving the cluster. At the same time, other lysosomes come to join the cluster. Very often, the departed lysosomes rejoin the original cluster. Averaging over  $\sim 75$  clusters, we obtain the rate of clustering, i.e., the rate of forming physical bonds between two lysosomes, to be  $k_{\text{cluster}} = 0.5 \text{ s}^{-1}$ . Based on the global state of the cell (the number of free and the number of clustered lysosomes) and assuming equilibrium, we can find the equilibrium constant for the clustering-declustering processes,  $\Omega = k_{\text{cluster}}/k_{\text{de-cluster}}$ . Here  $\Omega = 4$ , and hence the rate of declustering is  $k_{\text{de-cluster}} = 0.125 \text{ s}^{-1}$ .

### Transfer of polyplexes from endosomes to lysosomes

When polyplexes are inside endosomes and lysosomes, they display transport patterns according to the parameters reported above. To determine the rate of transfer from endosomes to lysosomes,  $k_{\text{tr}}$ , we examine the colocalization of Oregon green labeled PEI-DNA (in endosomes) with rhodamine-immunolabeled lysosomes as a function of time, post-transfection. Quantitative measurements allow us to capture the increasing fraction of PEI-DNA present in lysosomes (Fig. 4 *c*). The data are averaged over each cell, and over multiple cells at each time point. The curve is modeled with a first-order reaction to yield  $k_{\text{tr}} = 1/500 \text{ min}^{-1}$ . This is the global transfer rate. The local transfer rate will depend on the local concentration of lysosomes,  $c_L$ .

### Physiochemical properties of polyplexes after endosomal escape

The parameters which describe the processes after endosomal escape are adapted from the literature, including the

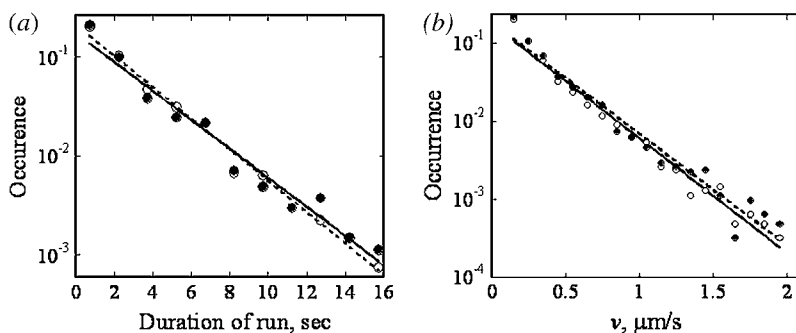


FIGURE 3 Transport properties of endosomes. (*a*) Distribution of the duration of runs of endosomes in the plus (solid circles) and minus (open circles) directions and (*b*) distribution of the frame-to-frame velocities in plus (solid circles) and minus (open circles) directions. The vertical coordinate indicates the frequency of occurrence of an event, i.e., the probability of observing a certain run-length (*a*) or a certain velocity (*b*).



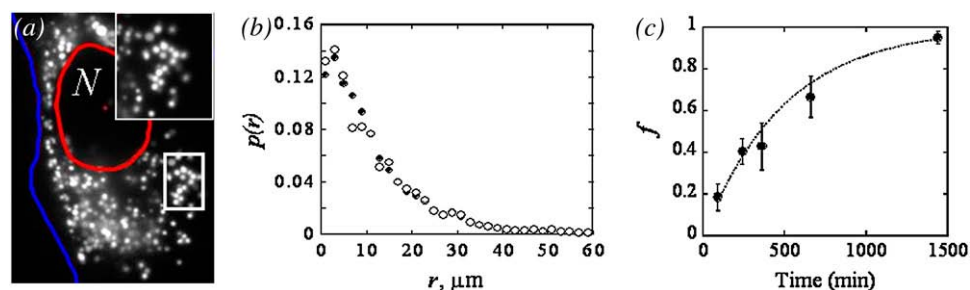


FIGURE 4 Intracellular spatial distribution of lysosomes and transfer of PEI-DNA from endosomes to lysosomes. (a) Fluorescent micrograph of lysosomes labeled by incubation of human dermal fibroblasts with fluorescent dextran for 2 h followed by a 22-h chase in culture medium. The nuclear and cell membrane are traced for clarity. Inset shows typical clusters of perinuclear lysosomes. (b) Spatial distribution of lysosomes represented by  $p(r)$ , the probability of finding a lysosome at a distance  $r$  from the nucleus. (c) Gradual delivery of PEI<sup>25</sup>-DNA vectors from endosomes to lysosomes. The ordinate is the fraction of total intracellular PEI<sup>25</sup>-DNA vectors that colocalize with LAMP1 positive structures (lysosomes) at different times post-transfection. Lysosomal delivery is seen to be substantially complete at 24 h post-transfection. The shaded line is a first-order kinetic fit on the data yielding  $k_{\text{transfer}} = 1/500 \text{ min}^{-1}$ .

rate of DNA degradation (15), the diffusivity of vector in the cytoplasm (17), the rate of unpacking (18), and the rate of binding of the vector to the nucleus (19) (see Supplementary Material, Table S4).

## MODEL VALIDATION

The stochastic model spans several length and timescales, as discussed above. The model is therefore validated at three separate levels against: 1), exact solution of single vesicle transport on single filament at timescales of 100 s; 2), experimental measurements of mean-squared displacements of endosomes in a live cell at timescales of 100 s; and 3), whole-cell-level spatial distribution of PEI<sup>25kDa</sup>-DNA vectors over 24 h. Comparisons of model predictions to gene expression data are given in Supplementary Material, section 2.5.

### Comparison with diffusion-reaction-advection models

To verify that the stochastic algorithm was implemented properly, we simulate movements of endosomes along a single, fixed filament. Transport of endosome obeys the transition map depicted earlier (see Table 2). The endosome is initially located at  $x = 0$ . The spatial movements of the endosomes in time are characterized by  $p(x,t)$ , the probability that an endosome is located at position  $x$  at time  $t$ . This probability can be theoretically predicted by a system of one-dimensional diffusion-advection-reaction equations (20).

Readers are referred to Supplementary Material in section 1.7 for more information on the diffusion-advection-reaction equations. In Fig. 5 *a*, we compare  $p(x,t)$  predicted by stochastic simulation (sampling of positions of 5000 particles) to the exact solution provided by diffusion-reaction-advection equations, for  $t = 50 \text{ s}$  and  $100 \text{ s}$ . The good agreement between simulation and analytical solution confirms that the stochastic algorithm is capable of accurately predicting transport mediated by molecular motors.

### Comparison with measured mean-square displacements of endosomes

We simulate movements of endosomes in two-dimensional cultured fibroblasts. The cell geometry is accurately reproduced from phase contrast images, and the MTOC is assigned a random location near the nucleus. The microtubules grow radially from the MTOC and exhibit dynamic instability, thus mimicking the real cells. A comparison between the predicted MSD and the measured MSD is shown in Fig. 5 *b*. At short times ( $t < 1 \text{ s}$ ), simulations show that vesicle motion is ballistic, as also seen in experiments ( $t^\gamma, \gamma \approx 2$ ). However, at long times ( $t > 10 \text{ s}$ ), particle motion exhibits diffusive scaling ( $t^1$ ) and may be described by an effective diffusive coefficient,  $D^{\text{eff}}$ . Kulkarni et al. reported similar observations (21). Over short timescales, vesicles experience limited runs and the mean velocity is nonzero and directional. However, at long times, vesicle motion is averaged over several random (in magnitude and direction) ballistic

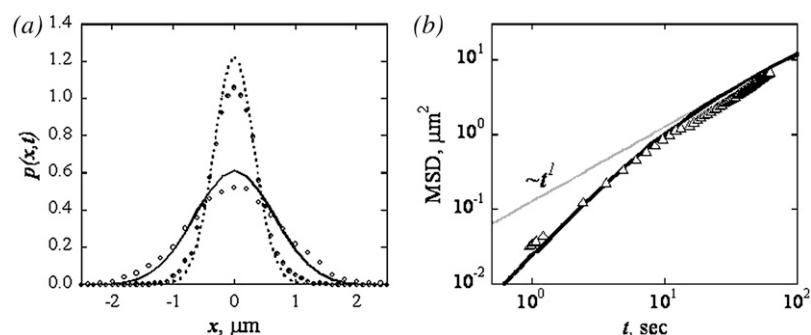


FIGURE 5 Model validation. (a) Displacement probability  $p(x,t)$  of a particle engaging in motor-assisted transport along a filament at  $t = 25 \text{ s}$  (solid line, exact solution; open circles, simulation) and  $t = 100 \text{ s}$  (dashed line, exact solution; solid circles, simulation). (b) Average mean-squared displacement for stochastically generated trajectories (solid line) and the experimentally measured trajectories (triangle). A crossover from subballistic to diffusive regime occurs between  $t = 10\text{--}100 \text{ s}$ .



runs and pauses, and exhibits a diffusionlike behavior. The simulation captures the essential physics of microtubule-dependent transport.

We observe that  $D^{\text{eff}}$  depends strongly on the density and the stability of microtubules. Decrease in the number of microtubules,  $N_{\text{MT}}$ , and increase in the frequency of catastrophe,  $f_{\text{cat}}$ , substantially reduce  $D^{\text{eff}}$  and cause accumulation of endosomes in the periphery. The effects of microtubule organization on gene delivery have been discussed in detail elsewhere (22). It should be noted that the effects of microtubule density and stability on the overall delivery efficiency are not significant for the ranges of parameters under consideration.

### Comparison with measured spatial distribution of PEI<sup>25kDa</sup>-DNA vectors—phases of perinuclear accumulation—cytoplasmic versus supranuclear vectors

The model was applied to predict the spatio-temporal distribution of PEI<sup>25kDa</sup>-DNA complexes that are present within endocytic vesicles. Prediction of the spatial distribution of vectors in dermal fibroblasts at 30 min, 4 h, and 11 h post-transfection (Fig. 6, *lower panel*) shows excellent qualitative agreement with experimental images (Fig. 6, *upper panel*). Looking from the top, the cell cytoplasm was divided into two regions—1), supranuclear; and 2), cytoplasmic—which are separated by the nuclear boundary. The supranuclear region is a thin layer of 2–4  $\mu\text{m}$  in width directly above the nucleus. Polyplex distributions in these two regions were treated separately.

We also performed a quantitative comparison of model predictions with experimental data by calculating normalized polyplex concentration  $c(r,t)$  (the number of polyplexes per unit area at a distance  $r$  from the nuclear membrane at time  $t$  post-transfection). The predicted polyplex concentration is within  $\pm 10\%$  of the experimental data (Fig. 7). This is encouraging since we do not use any fitting and all parameters are either measured or adapted from literature.

Initially, the polyplexes are dispersed uniformly in the cell due to random sites of endocytosis on the cell membrane ( $c(r,t=0) = 1$ , Fig. 7 *a*) and accumulate near the nucleus with time. Perinuclear accumulation of polyplexes occurs in two distinct phases (Fig. 7 *b*,  $c_{\text{peri}}(t)$ ). During the first phase, the average concentration of complexes in the perinuclear region quickly doubles within 1–2 h. This rapid accumulation is due to facilitated diffusion of endosomes containing PEI-DNA complexes on MTs as discussed above. Consequently, the complexes gradually disperse along the MTs. Since MTs are organized in an asterlike fashion, a uniform distribution on MTs leads to a higher concentration of polyplexes in the perinuclear region (23). The timescale over which the first phase of accumulation occurs depends upon the size of the cell and the MT-based effective diffusivity. The second phase of perinuclear accumulation is much slower, with a timescale of 6–10 h, and arises from gradual transfer of complexes from endosomes to lysosomes (Fig. 4 *c*). Delivery to lysosomes immobilizes (and hence concentrates) the polyplexes in perinuclear clusters (Fig. 7 *b*,  $c_{\text{peri}}(t)$ ). Thus, perinuclear accumulation of complexes arises not from any active targeting, but from the transport processes inherent to endocytic trafficking. The model, based on

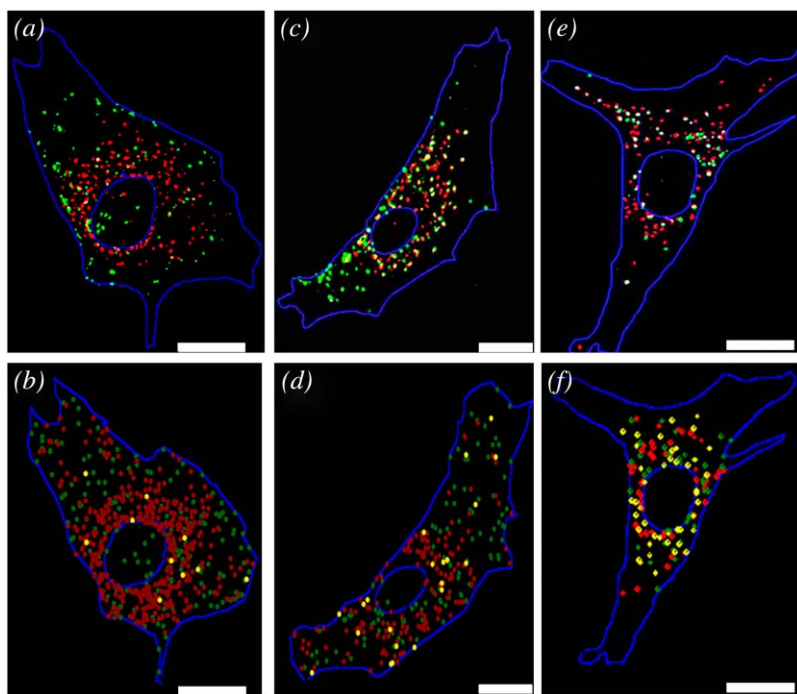


FIGURE 6 Comparison of model predictions (*lower panel*) of spatiotemporal distribution of PEI-DNA complexes to experimental data (*upper panel*). PEI-DNA complexes are labeled with Oregon green (*green*) and lysosomes are immunolabeled with rhodamine-X labeled secondary antibody (*red*). The yellow regions represent PEI-DNA vectors that colocalize with lysosomes. The same cells are reconstructed using simulations and presented in lower panel. The three cells correspond to (*a*, *b*) 30 min, (*c*, *d*) 4 h, and (*e*, *f*) 11 h post-transfection.

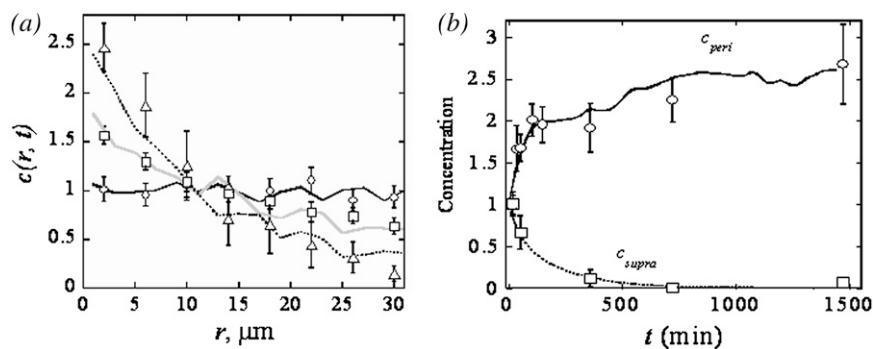


FIGURE 7 Validation of the model against experimental measurement of spatio-temporal distribution of PEI<sup>25kDa</sup>-vectors. (a) Normalized local concentration  $c(r,t)$  of vectors measured experimentally (symbols) and predicted by the model (lines) at 10 min (circles), 2 h (squares), and 24 h (triangles). The abscissa is  $r$ , the distance from the nucleus. The distributions are sampled from 20 cells. (b) The temporal evolution of vector concentration in the supranuclear region (squares) and the perinuclear region (circles). The perinuclear region is defined as a region of width 2  $\mu\text{m}$  around the nucleus. The lines are the predicted distributions.

fundamental interactions between vesicles and microtubules, is able to predict the spatio-temporal distribution of polyplexes, which evolve at much longer timescales.

In the supranuclear region, the density of MTs is low and most polyplexes do not exhibit MT-based transport. Supranuclear endosomal polyplexes diffuse slowly toward the perinuclear region, are transferred to lysosomes, and become immobilized in the perinuclear clusters. Effectively, polyplexes are transported out of the supranuclear region (Fig. 7 b,  $c_{\text{supra}}(t)$ ). The model accurately predicts the temporal evolution of vector concentration in the supranuclear region. The excellent agreement between the measured and calculated values of  $c(r,t)$ ,  $c_{\text{peri}}(t)$ , and  $c_{\text{supra}}(t)$  is a strong indication of the model's capability to predict transport of polyplexes inside cells.

## MODEL PREDICTIONS

The model was first used to examine the individual steps of the gene delivery pathway. The entire pathway was divided into two stages: 1), before endosomal/lysosomal escape, when the transport of vectors is determined by the endocytic vesicles; and 2), after endosomal escape, when the transport is determined by diffusion and stability of the vector. We first calculate the optimal location and time of endosomal escape that maximizes the probability of completing DNA delivery for in vitro cells. We then use this knowledge to predict the optimal pathways for in vitro and in vivo cells. Due to the complexity and multidimensionality of the parameter space, a global optimization of all parameters involved is not

possible. Instead, we develop a more intuitive procedure to find the optimal set of parameters.

## Optimal location of endosomal escape

After escape from endocytic vesicles, polyplexes must unpack to release the plasmid, which can then enter the nucleus. Diffusion coefficients of polyplexes and plasmids in the cytoplasm are small,  $10^{-4} \mu\text{m}^2/\text{s}$  and  $10^{-3} \mu\text{m}^2/\text{s}$ , respectively (17). While the polyplex is chemically stable, the plasmid is susceptible to cytoplasmic nucleases and has a short half-life ( $\sim 50$ – $90$  min) (15). Thus, only those plasmids that are close to the nucleus have a reasonable chance of success. To quantify this effect, we calculate the probability,  $\Phi(r)$ , that a polyplex, having escaped from an endocytic vesicle at distance  $r$  from the nuclear boundary at time  $t$ , will successfully deliver DNA to the cell nucleus (Fig. 8 a) (see Supplementary Material for mathematical definition of  $\Phi(r)$ ). The success probability  $\Phi(r)$  decreases as vectors escape away from the cell center, which is located at  $r = -5 \mu\text{m}$ . The value  $\Phi(r)$  is generally high for supranuclear escape ( $r < 0$ ) and declines only slightly toward the nuclear boundary ( $r = 0 \mu\text{m}$ ). On the contrary, for vectors that escape within the cytoplasmic region ( $r > 0$ ), the probability decreases exponentially with  $r$ , and at  $r = 1 \mu\text{m}$ ,  $\Phi(r)$  is already reduced to mere 0.01 (that is, 1%). The prediction that success probability is low for vectors that escape far away from the nucleus is intuitive. However, predictions in Fig. 8 a provide significant new information. First, they provide a quantitative determination of how success probability

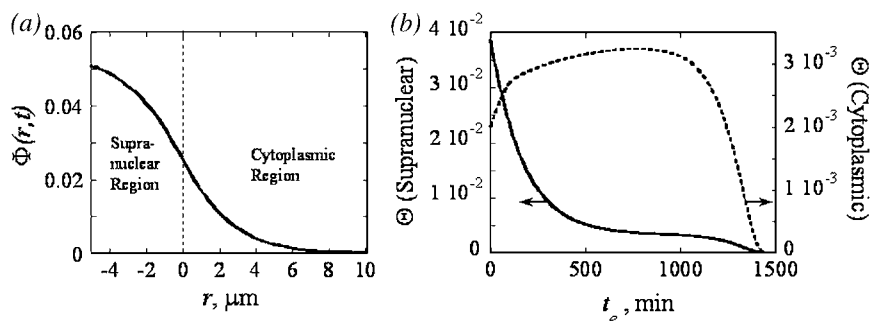


FIGURE 8 Likelihood of successful DNA delivery. (a) The value  $\Phi(r,t)$ , the probability that a vector, which escapes at a distance  $r$  from the nucleus at time  $t$ , will reach the nucleus. The probability is evaluated at 24 h after the occurrence of the escape event ( $r > 0$ , cytoplasmic region;  $r < 0$ , supranuclear region). (b) The value  $\Theta(t_e)$ , the probability that a vector, initially located in the supranuclear (solid) or cytoplasmic (dotted) region, completes DNA delivery to the nucleus at 24 h after escape from endosome or lysosome at time  $t_e$ .

decreases with distance. Second, they provide a direct means of comparing the contribution from supranuclear and cytoplasmic vectors. This will become important in discussing in vitro transfection experiments in which the supranuclear region often occupies a significant fraction of the cell (discussed later).

### Optimal time of escape

A similar analysis was performed with respect to time of escape,  $t_e$ . Specifically, we calculated the probability  $\Theta(t_e)$  that a vector escaping at time  $t_e$  post-transfection reaches the nucleus within 24 h (see Supplementary Material for mathematical definition of  $\Theta(t_e)$ ).  $\Theta(t_e)$  is essentially a spatially averaged value of  $\Phi(r)$  for all vectors released in the cytoplasm at time  $t_e$ . As seen in Fig. 8 b,  $\Theta(t_e)$  is very different for supranuclear and cytoplasmic vectors. For supranuclear vectors,  $\Theta(t_e)$  decreases monotonically with  $t_e$  as the vectors are gradually transported out of the supranuclear region due to endosome-lysosome fusion (Fig. 7 b,  $c_{\text{supra}}$ ). For cytoplasmic vectors,  $\Theta(t_e)$  exhibits an optimum in  $t_e$  at  $\sim 12$ – $13$  h post-transfection. If endosomal escape occurs too early, when most of the cytoplasmic vectors are far away from the nucleus, the released vectors will degrade before reaching the nucleus. On the other hand, late escape also results in low delivery efficiency. First, the longer the vectors stay inside endocytic vesicles, the more likely they will unpack and degrade inside lysosomes. Second, the released vectors may not have sufficient time to find and to enter the nucleus before the simulation is terminated. The precise contribution of each effect to the existence and the actual value of optimal escape time depend on several parameters.

The data in Fig. 8 b provides several new insights into transport of gene vectors. First, it clearly establishes that the best strategy for supranuclear vectors is to escape as early as possible. On the other hand, there exists a clear optimum escape time for cytoplasmic vectors. But most importantly, the data reveals that due to the stark differences between the behavior of supranuclear and cytoplasmic vectors, the geometry of the cell must be taken into account while determining the optimal escape time. Different cell lines have different sizes of nucleus and nucleus area to cell area ratios. These factors must be taken into account while comparing data from different cell lines.

### Global optimization of vector trafficking in vitro

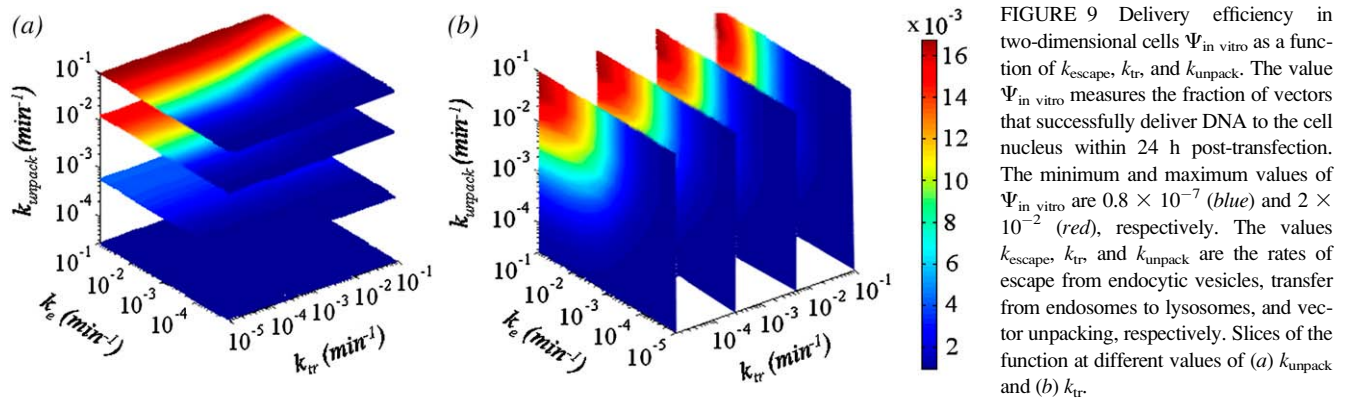
We next combined the data from the previous two sections and determined an overall efficiency  $\Psi$ , the probability that a vector released anywhere within the cell at any time delivers DNA to the nucleus. We then sought to determine vector parameters that optimize  $\Psi$ . We first defined the possible ranges of the parameter values that polyplexes are expected to possess. The parameter space is highly multidimensional, and consequently full optimization is computationally de-

manding. Instead, we followed a more intuitive path to reach the global maximum. The delivery efficiency exhibits a simple monotonous relationship with many parameters, e.g., rates of internalization and DNA degradation. We maximized these parameters to reach a semi-optimal state, around which we performed local optimization within a lower dimensional parameter space. We focused on a three-dimensional region of the parameter space represented by  $k_{\text{escape}}$  (the rate of vector escape from endosomes or lysosomes),  $k_{\text{tr}}$  (the rate of vector transfer from endosomes to lysosomes), and  $k_{\text{unpack}}$  (the rate of vector unpacking, and consequently plasmid degradation either in lysosomes or in the cytoplasm). These parameters account for the delicate balance between endocytic trafficking, endosomal escape, and vector stability. All other vector parameters were held at their respective optima. It is important to note that the parameters under consideration are both vector-specific and cell-specific. For instance, our experiments show that the rate of transfer from endosomes to lysosomes in human fibroblasts,  $k_{\text{tr}}$ , depends strongly on the nature of the internalized cargo:  $k_{\text{tr}}$  for dextran, polylysine-DNA vectors, and PEI<sup>25kDa</sup>-DNA vectors is  $1/45 \text{ min}^{-1}$ ,  $1/60 \text{ min}^{-1}$ , and  $1/600 \text{ min}^{-1}$ , respectively. Molecular conjugation of gene vectors with proper ligands will significantly alter the value of  $k_{\text{tr}}$ . The other parameters, e.g.,  $k_{\text{degL}}$ ,  $k_{\text{escape}}$ , and  $k_{\text{unpack}}$ , show the same dependency on the physicochemical properties of the vectors.

Under in vitro conditions (flat, adherent, two-dimensional geometry), optimization yielded relatively straightforward results, that is, vectors that escape early lead to high delivery. Supranuclear vectors have a much greater chance of success by virtue of their advantageous location. The relative number of supranuclear and cytoplasmic vectors depend on the ratio of nuclear area to the cell area. For cells with this ratio  $>0.06$  (which is true for most cells), the contribution of supranuclear vectors  $\Psi$  is dominant. Hence, high rate of escape and unpacking maximizes efficiency (Fig. 9). Standard PEI<sup>25kDa</sup> polyplexes, however, are far away from this maximal delivery state. The calculations show that the ratio of the maximum efficiency  $\Psi_{\text{max}}^{\text{in vitro}}$  to the base state ( $\Psi_{\text{PEI}^{25\text{kDa}}}^{\text{in vitro}}$ ) is  $\sim 80$ . Note that this enhancement ratio is based only on optimization of the intracellular pathway. Other factors such as toxicity of the polymer are not considered here.

### Global optimization of vector trafficking in vivo

In contrast to in vitro situations, cells under in vivo conditions are highly three-dimensional (24) and of a stellate shape, with a large central spherical portion (Fig. 1 b). Under these conditions, no region of the cell membrane is particularly close to the nuclear membrane. Due to this major difference in cellular morphology, the spatiotemporal distribution of vectors and hence optimal polyplex parameters are radically different from that in vitro. Fig. 10 depicts the predicted the spatial distribution of polyplexes in three-dimensional cells at 10 min, 4 h, and 24 h post-transfection,



calculated using the assumption that the principles and the parameters underlying endocytic trafficking are the same as those in vitro. At short times, there are no vectors within 2  $\mu\text{m}$  of the nucleus. All vectors are located close to the cell membrane, far-away from the nucleus. They are then gradually delivered to the perinuclear region by means of MT-dependent transport of endosomes, and endosome-to-lysosome transfer.

Fig. 11 shows optimization of vector properties for in vivo gene delivery. Optimal efficiency is observed at intermediate values of transfer and escape rate. The ratio of the maximum efficiency  $\Psi_{\text{max}}^{\text{in vivo}}$  to the base state ( $\Psi_{\text{PEI}^{25\text{kDa}}}^{\text{in vivo}}$ ) is  $\approx 40$ . Early escape of vectors from endosomes leads to underutilization of the endocytic trafficking and consequently, reduces perinuclear accumulation of the vectors, whereas a prolonged delay of vector escape promotes lysosomal degradation of the vector. Similarly, fast unpacking causes premature degradation of DNA inside lysosomes and cytoplasm, whereas slow unpacking limits the amount of DNA available for nuclear translocation. Interestingly, the optimal values of  $k_{\text{escape}}$  and  $k_{\text{unpack}}$  are functions of  $k_{\text{tr}}$ . Thus, to arrive at the

optimum pathway, the rates of unpacking and escape cannot be tuned independently but are constrained by  $k_{\text{tr}}$ .

### Impact of polymer degradability on gene delivery

Another important factor in the overall delivery efficiency is the stability of the polymer itself. The foregoing analysis is applicable to nonbiodegradable vectors like  $\text{PEI}^{25\text{kDa}}$ , which are immune to hydrolases, proteases, and nucleases, and offer a great degree of protection to their genetic cargo. For these vectors, it is reasonable to assume that the degradation of DNA is possible only after the vector unpacks. The stability of DNA in both the lysosomes and the cytoplasm is then intimately coupled to the rate of vector unpacking. On the other hand, biodegradable polymers such as poly( $\beta$ -amino esters) can themselves undergo hydrolysis in the lysosomes or the cytoplasm. The DNA can thus be degraded without the need to unpack. In other words, there is no direct coupling between unpacking and DNA lysosomal degradation. Surprisingly, this latter case, which makes the DNA more susceptible to enzymatic attacks, leads to an optimal pathway slightly more efficient than that for nonbiodegradable polymers (0.6% vs. 0.4% for in vivo applications). This higher efficiency stems from the inherent flexibility afforded to design of biodegradable polyplexes. Since DNA degradation in lysosomes is no longer conditional upon unpacking of the polyplex, it can be independently optimized as another parameter. Under these circumstances, the efficiency varies linearly with the rate of unpacking  $k_{\text{unpack}}$  and rate of degradation in lysosomes  $k_{\text{degL}}$ , and no optima exist with respect to these parameters (Supplementary Material, section 2.5).

### Impact of cell shape on gene delivery

Fig. 12 shows the effects of the shape and the size of in vitro cells on  $\Psi$ . The shape of the cell is characterized by its circularity and size. The circularity  $C$  is defined as  $C = 4\pi(A/P^2)$ , where  $A$  is the area of the cell and  $P$  is the perimeter. A small value of  $C$  indicates that the cell is elongated. The size is defined as the average distance between the cell membrane and the nuclear membrane. Elongated (less circular) and

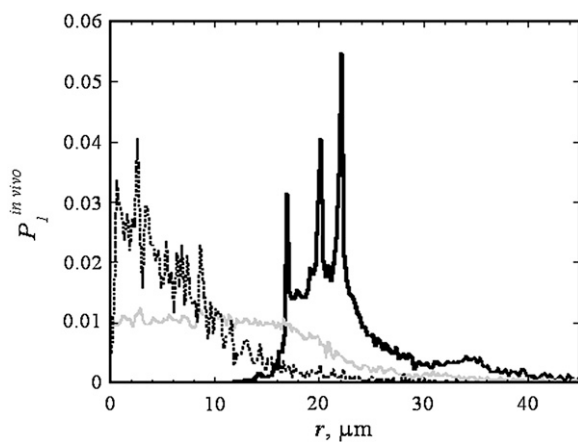
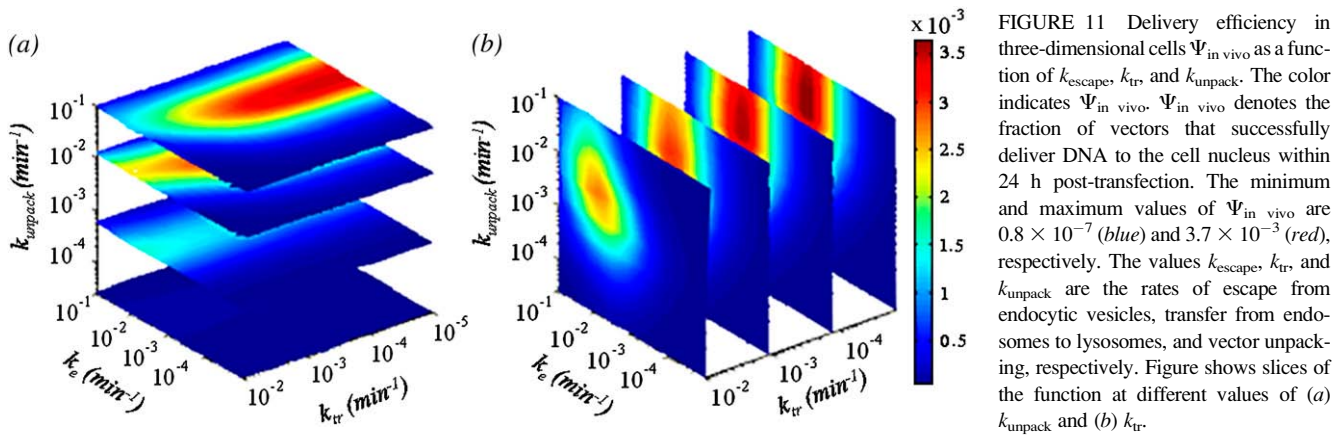


FIGURE 10 Spatiotemporal distribution of vectors in three-dimensional cells. Predicted spatial distribution of  $\text{PEI}^{25\text{kDa}}$ -DNA complexes in a three-dimensional cell at 10 min (solid), 4 h (shaded), and 24 h (dotted) post-transfection.  $P_I^{\text{in vivo}}$  is the probability that a vector is located at distance  $r$  from the nucleus at time  $t$  in a three-dimensional cell.





smaller cells have a larger fraction of the cell area nearer to the nucleus, leading to higher perinuclear concentration and hence a greater delivery efficiency. It is interesting to note that delivery efficiency can vary by almost an order of magnitude, only due to variation of shape and size of the cell.

## DISCUSSION

### Existing models versus current approach

Traditionally, gene delivery by synthetic vectors has been studied and modeled as biochemical reactions between the vectors and cellular components. With recent studies based on single-particle tracking, it has become evident that spatially heterogeneous transport processes are intimately in-

involved in every step along the delivery pathway (21,25). However, existing mathematical models of synthetic gene delivery approximate all transport processes by first-order kinetics (11,12,19). Such simple approximations not only undermine the predictability of the model but also fail to take advantage of data provided by microscopic experiments.

To overcome these issues, we introduced three new features in the present model. First, we introduced spatial coordinates to represent the cell geometry. The cell geometry is reconstructed directly from experimental images. Second, we follow the movements of single particles, just like in single-particle tracking experiments. Thus, intracellular trafficking of polyplexes is no longer represented as discrete jumps from one compartment to another, but as continuous movements of single particles. Third, we use stochastic algorithms to update the positions and the states of polyplexes and cellular organization. This is to reflect the inherent randomness of intracellular processes.

This approach has several advantages. First, it allows us to directly compare model predictions to experimental data. This proves to be crucial in not only model validation but also in verification of our understanding of underlying processes. Second, it enables us to develop a realistic and mechanistic description of intracellular transport phenomena. For instance, it accurately captures the basic physics of microtubule-dependent transport. The particles are allowed to switch intermittently between diffusion and motor-driven directional movements on MTs, just like what they do in experiments. Although the model requires several more parameters to characterize binding and detachment of particles to MTs, these parameters are real, have a physical meaning, and can be estimated directly from microscopic single-particle tracking experiments. Third, the stochastic algorithms grant us a great degree of flexibility in model implementation and solution methods, thus facilitating simultaneous representation of diverse physical and chemical processes that occur at multiple length and timescales. PDE-based models can describe spatially variable processes but are only restricted to simple and fixed cellular configurations. To obtain the

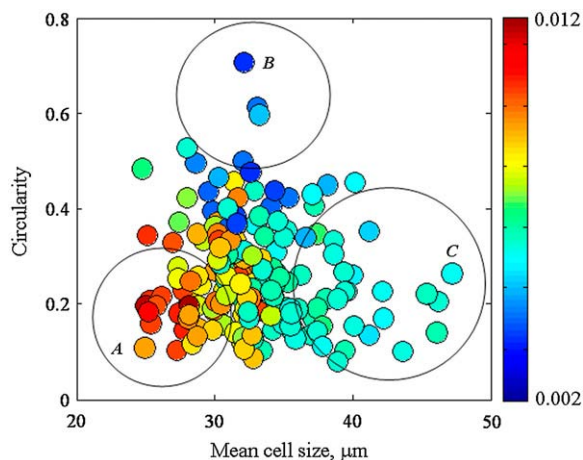


FIGURE 12 Effect of cell shape and size on the delivery efficiency  $\Psi_{in\ vitro}$  for dermal fibroblasts in culture. The color indicates  $\Psi_{in\ vitro}$ . The ratio between the maximum and minimum delivery efficiency is 6.2. The delivery efficiency increases with decreasing size and circularity. Low circularity often provides higher access to nucleus, hence the higher transfection efficiency. The circles denoted by A–C show three extremes in the circularity-size space that are captured by the cell population used. Note that  $k_{escape} = 0.15\ h^{-1}$ ,  $k_{tr} = 0.1\ h^{-1}$ ,  $k_{degL} = 0.042\ h^{-1}$ ,  $D_{DNA} = 10^{-3}\ \mu m^2/s$ ,  $k_{deg-cyto,DNA} = 1\ h^{-1}$ ,  $k_{nuc} = 1/4\ h^{-1}$ , and  $k_{unpack} = 0.25\ h^{-1}$ .

solutions to the transport equations for complex geometry and dynamic environment, stochastic simulations are far more superior. Fourth, the model provides an integrated framework to systematically study the influence of all model parameters and extract optimal parameter sets.

The model relates molecular-level binding and trafficking events to whole-cell distribution of polyplexes, and eventually to gene delivery efficiency. The mechanistic treatment of transport allows us to study the effects of cell geometry, motor-assisted transport and endocytic trafficking. For the first time, the spatiotemporal distribution of polyplexes before escape from endocytic vesicles can be predicted with great accuracy. This information is crucial to the design of better vectors.

Perhaps the most important feature of the model is that it represents a step toward a more realistic description of intracellular transport in general and gene delivery in particular. Many processes in gene delivery pathway—for example, endosomal escape and DNA degradation—are extremely difficult to measure experimentally in situ. Accordingly, mechanistically sound models provide a valuable tool in studying the impact of these processes on gene delivery. Such models also provide a logical platform for synthesis and integration of information from diverse sources, bridging scales, cell types, and operating conditions, and allow predictions of cellular and subcellular processes that are inaccessible by current experimental tools.

### New insights into gene delivery brought out by this model

The model presented here brings out several novel insights into mechanisms of gene delivery by polyplexes.

The model reveals, quantitatively, that the morphology of cells (e.g., size, shape, and dimension), which has been largely ignored in gene delivery research, strongly influences the delivery efficiency. This is significant since human cells exhibit a wide range of morphologies—muscle cells in the body are very flat and elongated, whereas dermal fibroblasts are stellate and round. It can be inferred from the model results that the strategies to be used for these two applications must be very different. In addition to the morphology of the cell, other cell-specific

properties such as endocytic trafficking and microtubule-dependent transport can also affect design decisions.

The most conspicuous example of impact of geometry is comparison of in vitro and in vivo cells. Traditionally, synthetic vectors are optimized in vitro, based on the assumption that they will also perform optimally under in vivo conditions. It is apparent from our study that such assumption can be erroneous, as not only the optimal parameters but also the pathway to reach the optima are remarkably different for those two conditions. Fig. 13 *a* shows the ratio of different vector-dependent parameters at the optimal states and the base states of PEI<sup>25kDa</sup>-DNA for gene delivery to dermal fibroblasts under in vitro and in vivo conditions. Under in vitro conditions, it is possible to have an unmitigated increase in the rates of escape and unpacking, while at the same time enhancing the delivery efficiency. For in vivo applications, the extent of increase of  $k_{\text{escape}}$  and  $k_{\text{unpack}}$  must be carefully controlled, lest the optima be overshoot. Fig. 13 *b* shows the position of the base state (PEI<sup>25kDa</sup>) and the conceptual route to the optimal pathway for in vivo applications. Overshooting the optimum in any direction can cause a significant reduction in the delivery efficiency (up to 1000-fold). Another interesting feature of Fig. 13 *a* is the difference in the optimal rate of transfer from endosomes to lysosomes,  $k_{\text{tr}}$ , under in vitro and in vivo conditions. While this rate does not play a major role in vitro, it plays an important role in vivo and must be reduced to maximize the delivery efficiency. Also, the optimal values of  $k_{\text{escape}}$  and  $k_{\text{unpack}}$ , as discussed earlier, are strongly dependent upon  $k_{\text{tr}}$ . It should be noted that  $k_{\text{tr}}$  depends upon the direct interaction of the vector with the endocytic machinery, mechanistic details of which are not well understood. In summary, synergistic considerations of these seemingly independent processes (i.e., endolysosomal escape, transfer to lysosomes, and vector unpacking) are necessary for improving delivery efficiency.

The model shows that under in vitro conditions, successful gene delivery is dominated by supranuclear vectors for a typical cell. This is interesting because supranuclear population of gene vectors is not as well studied as their cytoplasmic counterpart. The model implies that further detailed experimental studies are warranted on intracellular trafficking and the overall behavior of supranuclear vectors.

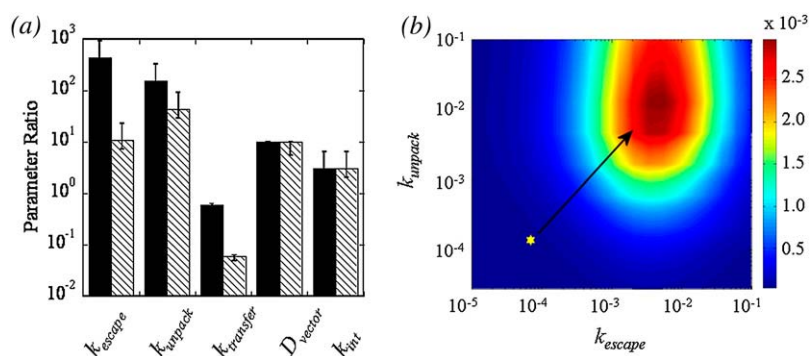


FIGURE 13 Design strategies to improve PEI<sup>25kDa</sup>-DNA polyplexes. (a) Ratio of different polymer-dependent parameters of the optimal solution to those of PEI<sup>25kDa</sup> for in vitro (solid bars) and in vivo (hatched bars) and (b)  $\Psi_{\text{in vivo}}$  as a function of  $k_{\text{unpack}}$  and  $k_{\text{escape}}$  for  $k_{\text{tr}} = 1/500 \text{ min}^{-1}$  (for PEI<sup>25kDa</sup>). The position of PEI<sup>25kDa</sup> is also indicated (yellow star). The arrow shows the trajectory to be followed to arrive at the optimum, assuming  $k_{\text{tr}}$  is held constant.

The model also makes a quantitative estimate of the extent to which synthetic vectors can be improved. As such, it complements a large number of experimental efforts focused on design and synthesis of new polyplexes. The model shows that PEI<sup>25kDa</sup>-DNA, the gold standard of synthetic vectors, is highly suboptimal, with delivery efficiency 20–100-fold less than optimal configurations. However, more interestingly, it predicts that even under optimal conditions, the calculated values of  $\Psi_{\text{in vivo}}^{\text{max}}$  and  $\Psi_{\text{in vitro}}^{\text{max}}$  are only 0.4% and 2%, respectively—significantly lower than the typical efficiency of viral vectors ( $\approx 10$ –100%). The prediction that there exists an upper limit on the delivery efficiency and that the upper limit is very low in comparison to viral vectors is very nonobvious, and has significant implications in assessing relative merits of viral and nonviral vectors.

The distinction between the viral and the synthetic gene delivery pathways is most apparent in the steps after endosomal escape. Specifically, the DNA delivered by polyplexes has to diffuse across the cytoplasm and find the nuclear pore complexes. Adenoviruses, on the other hand, are capable of recruiting molecular motors for fast, directed transport on MTs toward the nucleus and docking specifically on the nuclear pore complexes for final release of the viral DNA into the nucleus (22). Thus, the viral DNA is protected inside the viral capsids throughout this process. The post-escape success probability  $\Phi(r)$  for a polyplex is  $\sim 10^{-2}$  (Fig. 8 *a*), whereas for an adenovirus it is essentially 1. To break away from the upper limit of  $O(1\%)$  and attain the efficiency of viral vectors, fundamental changes in vector design are necessary. For instance, vectors that are capable of recruiting molecular motors will reduce cytoplasmic degradation. Our simulations show that a synthetic vector capable of traveling on microtubules after endocytic release but otherwise identical to the optimal vector can increase the delivery efficiency up to 8%, which is three orders-of-magnitude more than that of PEI<sup>25kDa</sup> (see Supplementary Material, section 2.4).

### Limitations of the model

The present modeling approach is a rough approximation to reality; however, it succeeds in providing a consistent and quantitative description of synthetic gene delivery at a cellular level, and lays a board foundation for further developments. Future experimental and theoretical studies are required to strengthen several assumptions employed in the model. Lack of knowledge, especially at the mechanistic level, limits the ability to quantify some effects, which may or may not be important. Three important factors that may influence comparison of model predictions to experimental data are briefly discussed here. First, the present model does not account for cooperative effects of vectors. For example, it is possible that more than one vector is present within a lysosome (26) and the rate of escape can depend upon polymer concentration in the vesicle in some nonlinear fashion. Second, the model does not account for toxicity of

polymers. It has been shown in many cases that reduction in toxicity of PEI<sup>25kDa</sup> by chemical modifications also increases the transfection efficiency (27). Third, the model only addresses DNA delivery to nondividing cells. The effects of mitosis will be addressed in more details in future work.

The algorithms used for stochastic simulations in this work represent the first step and require a great deal of computational resources. Recent advances in stochastic computing and random sampling can improve the performance of the algorithms and expedite the calculations (28,29). Implementation of such algorithms will facilitate the applications of the current approach to more complex systems, involving larger number of reactions and transport processes.

### CONCLUSIONS

In this study, we have developed a comprehensive and integrated computational framework for intracellular trafficking of polyplexes. The numerical values of the model parameters were adapted from previous reports in literature or directly measured from our experiments. Without any fitting, the model was able to predict the measured spatiotemporal distribution of polyplexed cultured fibroblasts with a reasonable agreement. We then use the model to predict the optimal intracellular itinerary that a vector should follow to achieve maximum delivery efficiency. The model yields two significant insights, among others. First, there exists a low upper limit on polyplexes' intracellular delivery efficiency; and the inability of the polyplex to protect its genetic cargo until the final point of nuclear entry is the root cause of this limited efficiency. Second, there is a strong influence of cell morphology on vector trafficking, mediated by the natural endocytic machinery of the cell. Thus, strategies for optimization of polyplexes for flat (two-dimensional) cells (e.g., in vitro monolayers, muscle cells) and round (three-dimensional) cells (e.g., in vivo fibroblasts, T-cells) are significantly different. For three-dimensional cells, the system behavior with respect to the two most important parameters, rates of endosomal escape and unpacking, is highly nonlinear and poses significant design challenges, which are more complicated than previously realized. The present analysis represents a critical step toward quantitative engineering design of polymer-based vectors.

### SUPPLEMENTARY MATERIAL

An online supplement to this article can be found by visiting BJ Online at <http://www.biophysj.org>.

### REFERENCES

1. Duncan, R. 2003. The dawning era of polymer therapeutics. *Nat. Rev. Drug Discov.* 2:347–360.
2. National Institutes of Health. 2006. Genetic Modification Clinical Research Information System (GeMCRIS). Protocol Numbers: 9703–9180, 0002–9378, 0104–9461. NIH, Bethesda, MD.



3. Medina-Kauwe, L. K., J. Xie, and S. Hamm-Alvarez. 2005. Intracellular trafficking of nonviral vectors. *Gene Ther.* 12:1734–1751.
4. Boussif, O., F. Lezoualc'h, M. A. Zanta, M. D. Mergny, D. Scherman, B. Demeneix, and J. P. Behr. 1995. A versatile vector for gene and oligonucleotide transfer into cells in culture and in vivo: polyethylenimine. *Proc. Natl. Acad. Sci. USA.* 92:7297–7301.
5. Akinc, A., D. M. Lynn, D. G. Anderson, and R. Langer. 2003. Parallel synthesis and biophysical characterization of a degradable polymer library for gene delivery. *J. Am. Chem. Soc.* 125:5316–5323.
6. Borchard, G. 2001. Chitosans for gene delivery. *Adv. Drug Deliv. Rev.* 52:145–150.
7. Pun, S. H., and M. E. Davis. 2002. Development of a nonviral gene delivery vehicle for systemic application. *Bioconjug. Chem.* 13: 630–639.
8. Watson, P., A. T. Jones, and D. J. Stephens. 2005. Intracellular trafficking pathways and drug delivery: fluorescence imaging of living and fixed cells. *Adv. Drug Deliv. Rev.* 57:43–61.
9. Forrest, M. L., and D. W. Pack. 2002. On the kinetics of polyplex endocytic trafficking: implications for gene delivery vector design. *Mol. Ther.* 6:57–66.
10. Varga, C. M., K. Hong, and D. A. Lauffenburger. 2001. Quantitative analysis of synthetic gene delivery vector design properties. *Mol. Ther.* 4:438–446.
11. Varga, C. M., N. C. Tedford, M. Thomas, A. M. Klibanov, L. G. Griffith, and D. A. Lauffenburger. 2005. Quantitative comparison of polyethylenimine formulations and adenoviral vectors in terms of intracellular gene delivery processes. *Gene Ther.* 12:1023–1032.
12. Banks, G. A., R. J. Roselli, R. Chen, and T. D. Giorgio. 2003. A model for the analysis of nonviral gene therapy. *Gene Ther.* 10:1766–1775.
13. Roth, C. M., and S. Sundaram. 2004. Engineering synthetic vectors for improved DNA delivery: insights from intracellular pathways. *Annu. Rev. Biomed. Eng.* 6:397–426.
14. Sept, D., H. J. Limbach, H. Bolterauer, and J. A. Tuszynski. 1999. A chemical kinetics model for microtubule oscillations. *J. Theor. Biol.* 197:77–88.
15. Lechardeur, D., K. J. Sohn, M. Haardt, P. B. Joshi, M. Monck, R. W. Graham, B. Beatty, J. Squire, H. O'Brodovich, and G. L. Lukacs. 1999. Metabolic instability of plasmid DNA in the cytosol: a potential barrier to gene transfer. *Gene Ther.* 6:482–497.
16. Komarova, Y. A., I. A. Vorobjev, and G. G. Borisy. 2002. Life cycle of MTs: persistent growth in the cell interior, asymmetric transition frequencies and effects of the cell boundary. *J. Cell Sci.* 115:3527–3539.
17. Lukacs, G. L., P. Haggie, O. Seksek, D. Lechardeur, N. Freedman, and A. S. Verkman. 2000. Size-dependent DNA mobility in cytoplasm and nucleus. *J. Biol. Chem.* 275:1625–1629.
18. Schaffer, D. V., N. A. Fidelman, N. Dan, and D. A. Lauffenburger. 1999. Vector unpacking as a potential barrier for receptor-mediated polyplex gene delivery. *Biotechnol. Bioeng.* 67:598–606.
19. Varga, C. M., K. Hong, and D. A. Lauffenburger. 2001. Quantitative analysis of synthetic gene delivery vector design properties. *Mol. Ther.* 4:438–446.
20. Smith, D. A., and R. M. Simmons. 2001. Models of motor-assisted transport of intracellular particles. *Biophys. J.* 80:45–68.
21. Kulkarni, R. P., D. D. Wu, M. E. Davis, and S. E. Fraser. 2005. Quantitating intracellular transport of polyplexes by spatio-temporal image correlation spectroscopy. *Proc. Natl. Acad. Sci. USA.* 102:7523–7528.
22. Dinh, A. T., T. Theofanous, and S. Mitragotri. 2005. A model for intracellular trafficking of adenoviral vectors. *Biophys. J.* 89:1574–1588.
23. Pangarkar, C., A. T. Dinh, and S. Mitragotri. 2005. Dynamics and spatial organization of endosomes in mammalian cells. *Phys. Rev. Lett.* 95:158101.
24. Beningo, K. A., M. Dembo, and Y. L. Wang. 2004. Responses of fibroblasts to anchorage of dorsal extracellular matrix receptors. *Proc. Natl. Acad. Sci. USA.* 101:18024–18029.
25. Suh, J., D. Wirtz, and J. Hanes. 2003. Efficient active transport of gene nanocarriers to the cell nucleus. *Proc. Natl. Acad. Sci. USA.* 100:3878–3882.
26. Mishra, S., P. Webster, and M. E. Davis. 2004. PEGylation significantly affects cellular uptake and intracellular trafficking of nonviral gene delivery particles. *Eur. J. Cell Biol.* 83:97–111.
27. Thomas, M., J. J. Lu, Q. Ge, C. Zhang, J. Chen, and A. M. Klibanov. 2005. Full deacylation of polyethylenimine dramatically boosts its gene delivery efficiency and specificity to mouse lung. *Proc. Natl. Acad. Sci. USA.* 102:5679–5684.
28. Cao, Y., L. R. Petzold, M. Rathinam, and D. T. Gillespie. 2004. The numerical stability of leaping methods for stochastic simulation of chemically reacting systems. *J. Chem. Phys.* 121:12169–12178.
29. Chatterjee, A., K. Mayawala, J. S. Edwards, and D. G. Vlachos. 2005. Time accelerated Monte Carlo simulations of biological networks using the binomial tau-leap method. *Bioinformatics.* 21:2136–2137.